



CHORUS

This is the accepted manuscript made available via CHORUS. The article has been published as:

Coherent detection of THz-induced sideband emission from excitons in the nonperturbative regime

K. Uchida, T. Otobe, T. Mochizuki, C. Kim, M. Yoshita, K. Tanaka, H. Akiyama, L. N. Pfeiffer, K. W. West, and H. Hirori

Phys. Rev. B **97**, 165122 — Published 13 April 2018

DOI: [10.1103/PhysRevB.97.165122](https://doi.org/10.1103/PhysRevB.97.165122)

1 **Coherent detection of THz-induced sideband emission from excitons**
2 **in the nonperturbative regime**

3 K. Uchida,¹ T. Otohe,² T. Mochizuki,³ C. Kim,⁴ M. Yoshita,³ K. Tanaka,^{1,5} H.
4 Akiyama,⁴ L. N. Pfeiffer,⁵ K. W. West,⁵ and H. Hirori^{5,7,*}

5 ¹*Department of Physics, Graduate School of Science, Kyoto University, Kyoto, Kyoto*
6 *606-8502, Japan*

7 ²*Kansai Photon Science Institute, National Institutes for Quantum and Radiological*
8 *Science and Technology, Kizugawa, Kyoto 619-0615, Japan*

9 ³*Fukushima Renewable Energy Institute, National Institute of Advanced Industrial*
10 *Science and Technology, Koriyama, Fukushima 963-0298, Japan*

11 ⁴*Institute for Solid State Physics, the University of Tokyo, Kashiwa, Chiba 277-8581,*
12 *Japan*

13 ⁵*Institute for Integrated Cell-Material Sciences (iCeMS), Kyoto University, Kyoto,*
14 *Kyoto 606-8501, Japan*

15 ⁶*Department of Electrical Engineering, Princeton University, Princeton, New Jersey*
16 *08544, USA*

17 ⁷*Institute for Chemical Research, Kyoto University, Uji, Kyoto 611-0011, Japan*

18 Strong interaction of terahertz (THz) wave with excitons induces nonperturbative
19 optical effects such as Rabi splitting and high-order sideband generation. Here, we
20 investigated coherent properties of THz-induced sideband emissions from
21 GaAs/AlGaAs multi-quantum-wells. With increasing THz electric field, optical
22 susceptibility of THz dressed exciton shows red shift with spectral broadening and
23 extraordinary phase shift. This implies that the field ionization of the 1s exciton
24 modifies the THz-dressed exciton in the nonperturbative regime.

25 PACS: 78.47.J-, 78.67.De, 42.65.Ky, 42.50.Hz

26 *hirori@scl.kyoto-u.ac.jp

I. INTRODUCTION

The coherent nonlinear interaction of intense light fields with electronic states in semiconductors gives rise to intriguing nonperturbative phenomena such as high-harmonic generation and optical-field-induced current [1-3], which possess electron dynamics that are highly sensitive to the driving phase of the laser [4]. These dynamics are characterized by light-matter interaction energy such as Rabi energy $\hbar\Omega_R$ and ponderomotive energy U_p . Rabi energy $\hbar\Omega_R$ describes coupling strength between electronic state and light, and ponderomotive energy describes time-averaged kinetic energy of electron under light field. When such light-matter interaction energies approach the same order of magnitude as transition energy of electronic state, rotating-wave approximation (RWA) and perturbation theory cannot be applied [5]. Excitons in semiconductors, which are hydrogen-like quasiparticles scaled energetically by 1/1000 compared with atomic systems, are attractive for studying the light-matter interactions in the presence of Coulomb interactions [6]. The intra-excitonic transitions have a large dipole moment and their energies lie in the terahertz (THz) range [7]. These properties allow us to reach a highly nonperturbative regime ($\hbar\Omega_R, U_p \sim \epsilon_{1s-2p}$: transition energy of exciton) with comparably moderate fields without breakdown of material.

Recent studies on the interactions between excitons and THz electric fields have revealed the Rabi splitting [8-10], the electric-field induced ionization [11,12], and the sideband emission [13-15]. In the previous work, the excitonic optical absorption of semiconductors in the presence of a THz wave has been modulated on a sub-cycle timescale [16,17]. We found that the output probe intensity was coherently reshaped by the sideband emissions from the THz-photon dressed state of exciton [17,18]. The modulation can be explained by the optical susceptibility which involves the energy spectrum of the THz-dressed excitons [19]. In the nonperturbative regime, it is well

1 known that the THz electric field induces excitonic ionization and high-order sideband
2 generation (HSG) [15,16]. As the ionization may modify the THz-dressed excitons, it is
3 crucial to determine the dependence of the susceptibility on the field strength for a
4 deeper understanding of the HSG in the nonperturbative regime, which is useful for
5 sub-cycle control and synthesis of optical pulses.

6

7 In this study, by using a heterodyne detection technique, we investigated the coherent
8 properties of the sideband emission from excitons and obtained the optical susceptibility
9 under intense THz wave illumination, which is directly related to the energy spectrum
10 of the THz-dressed excitons. The ground-state (1s) excitons in a GaAs/AlGaAs
11 multi-quantum-well (MQW) were excited by near-infrared (NIR) pulses and driven via
12 phase-stable multi-cycle THz pulses. The dependence of both the amplitude and phase
13 of the second-order sideband emission on the THz electric field implies that the field
14 ionization of the 1s exciton strongly modifies the energy spectrum of the dressed
15 exciton.

16

17 **II. EXPERIMENT**

18

A. Setup and sample

19 In our experiment, we utilized a THz electric field to drive the intra-excitonic
20 transition in a GaAs/AlGaAs MQW and a NIR pulse which excites the exciton
21 (exc-NIR pulse), and observed the sideband emissions from the MQW sample as
22 illustrated in Fig. 1 (a). The laser source was a Ti:sapphire regenerative amplifier
23 (repetition rate: 1 kHz, pulse energy: 4 mJ, central energy: 1.55 eV, pulse width: 100
24 fs). The NIR laser output was split to generate the NIR pulses and the THz driving
25 pulses with two separate beam paths. Single-cycle THz pulses were generated with a
26 LiNbO₃ crystal by using the tilted-pulse-intensity-front scheme and we converted them

1 into multi-cycle (narrowband) ones by using a bandpass filter [20,21]. Figures 1(b) and
 2 (c) show the temporal and the Fourier profiles of the THz pulse with a central energy of
 3 $\hbar\Omega = 2.5$ meV ($\Omega = 0.6$ THz) and a bandwidth of 0.4 meV (0.1 THz). A pair of wire
 4 grid polarizers (WGPs) was used to vary the amplitude of the THz electric field from
 5 0.4 to 16 kV/cm without changing its temporal profile. The NIR pulses were passed
 6 through a pulse shaper consisting of a grating, lens, and a single-slit mask to obtain a
 7 narrowband and wavelength-tunable exc-NIR pulse (see Sec. II-B). When a double-slit
 8 mask is inserted in the pulse shaper, two NIR pulses with different color are obtained,
 9 and the high-energy photons can be used as a reference (ref)-pulse in the heterodyne
 10 detection explained later (see Sec. II-C). The NIR pulses that was transmitted through
 11 the sample was analyzed by a spectrometer with an energy resolution of 0.3 meV and
 12 detected with a charge-coupled-device (CCD) camera.

13

14 In our experiment, we used a GaAs/AlGaAs MQW sample that consisted of ten
 15 periods of 12-nm-wide GaAs wells separated by 10-nm-wide $\text{Al}_{0.3}\text{Ga}_{0.7}\text{As}$ barriers
 16 grown on a semi-insulating GaAs (100) substrate with molecular beam epitaxy. To
 17 enable optical transmission measurements, the GaAs substrate was removed by
 18 chemical etching and attached to a SiO_2 substrate. The sample was placed in a cryostat
 19 and the temperature during the experiments was set to 10 K. Figure 1(d) shows the
 20 absorption spectrum of the GaAs/AlGaAs MQW at 10 K. The dominant peak at
 21 $\epsilon_{1s} = 1.55$ eV is attributed to the 1s state of the heavy-hole (HH) exciton. From the 2s-HH
 22 exciton peak observed at higher energies, the 1s-2p transition energy ϵ_{1s-2p} is estimated
 23 to be 8 meV, which is larger than $\hbar\Omega$ and thus we have a non-resonant driving of the
 24 excitonic system in our experiment.

25

26 **B. Measurement of the sideband emission intensity**

1 The schematic energy diagram of the excitonic system without THz illumination is
 2 shown on the left-hand side in Fig. 2(a), and the right-hand side illustrates THz-dressed
 3 excitonic system caused by the THz wave illumination. The eigenstates of the dressed
 4 exciton are separated by even multiples of the THz photon energy $\hbar\Omega$ ($\epsilon_{\text{exc}} + 2n\hbar\Omega$ with
 5 n being an integer). When the dressed exciton is excited by the exc-NIR pulse with the
 6 energy of $\hbar\omega_{\text{exc}}$, the THz-induced $2m^{\text{th}}$ -order sideband (hereafter referred to as $2m^{\text{th}}$
 7 sideband) emissions can be observed ($\hbar\omega_{\text{exc}} + 2m\hbar\Omega$ with m being an integer). Figure
 8 2(b) shows the sideband spectrum obtained for simultaneous excitation with the
 9 exc-NIR pulse ($\hbar\omega_{\text{exc}}$ resonant with $\epsilon_1=1.55$ eV) and the THz wave ($E_{\text{THz}} = 10$ kV/cm).
 10 The orange solid lines are the three emission peaks of the $\pm 2^{\text{nd}}$ and $+4^{\text{th}}$ sideband.

11
 12 In our experiment, the field strength of exc-NIR pulse E_{exc} is sufficiently weak, and
 13 thus the complex electric field amplitude of the $2m^{\text{th}}$ sideband emission E_{2m} is linearly
 14 proportional to the field E_{exc} , and can be described in the frequency domain with

$$16 \quad E_{2m}(\omega_{\text{exc}} + 2\Omega) = C_{2m}(\omega_{\text{exc}}, E_{\text{THz}}, \Omega) E_{\text{exc}}(\omega_{\text{exc}}). \quad (1)$$

17
 18 Here, the complex coefficient $C_{2m}(\omega_{\text{exc}})$ is proportional to the optical susceptibility
 19 $\chi_{2m}(\omega_{\text{exc}})$ under THz wave illumination, and is directly related to the energy spectrum of
 20 the THz dressed exciton [18]. The components of $C_{2m} = |C_{2m}| \exp(i\theta_{2m})$ reflect the
 21 amplitude ratio ($|C_{2m}| = |E_{2m}/E_{\text{exc}}|$) and phase difference ($\theta_{2m} (= \arg(E_{2m}/E_{\text{exc}}))$) between
 22 the $2m^{\text{th}}$ sideband emission and the exc-NIR pulse. The squared amplitude $|C_{2m}|^2$
 23 indicates sideband intensity efficiency, and can be estimated from the intensity of the
 24 sideband emission as shown in Fig. 2(b), e.g., $|C_{+2}|^2 \approx 10^{-3}$ at a THz electric field
 25 strength of 10 kV/cm. However, we cannot access the phase information θ_{2m} with this
 26 simple measurement.

1

2

C. Heterodyne detection technique

3

4

5

6

7

8

9

$$\tilde{E}_{\text{THz}}(t) = \frac{1}{2} E_{\text{THz}} \exp(i\Omega t) + c.c., \quad (2)$$

$$\tilde{E}_{\text{NIR}}(t) = \frac{1}{2} \{ E_{\text{exc}} \exp[i\omega_{\text{exc}}(t-\tau)] + E_{\text{ref}} \exp[i(\omega_{\text{exc}} + 2m\Omega)(t-\tau)] \} + c.c., \quad (3)$$

12

13

14

15

16

17

18

19

20

21

22

23

24

25

26

In order to access the complex coefficient C_{2m} of the $2m^{\text{th}}$ sideband emission with high sensitivity, we utilized a heterodyne detection technique. By using a double-slit mask in the pulse-shaper, a two-color NIR pulse with photon energies of $\hbar\omega_{\text{exc}}$ and $\hbar\omega_{\text{ref}}$ ($= \hbar\omega_{\text{exc}} + 2m\hbar\Omega$) can be produced as depicted in Fig. 3(a). The high-energy photons ($\hbar\omega_{\text{ref}}$) were used for the ref-NIR pulse in the heterodyne detection. Here, for simplicity, we assume continuous THz and NIR waves, which can be described by

where τ is the time delay between the THz and NIR pulses, and E_{ref} is the electric field amplitude of the ref-NIR pulse. As shown in Fig. 3(b), the time delay τ in Eq. (2) is defined with the time difference between the maximum-peak positions of the THz and NIR pulses.

The ideally transmitted NIR intensity I_{tot} (at $\hbar\omega_{\text{exc}} + 2m\hbar\Omega$) detected after the sample is a combination of the $2m^{\text{th}}$ sideband emission and the ref-NIR wave. By using Eqs. (1) and (3), I_{tot} as a function of the time delay τ can be written as

$$\begin{aligned} I_{\text{tot}}(\omega_{\text{exc}} + 2m\Omega, \tau) &\propto |E_{\text{ref}} \exp[-i(\omega_{\text{exc}} + 2m\Omega)\tau] + C_{2m} E_{\text{exc}} \exp[-i\omega_{\text{exc}}\tau]|^2 \\ &= E_{\text{ref}}^2 + |C_{2m}|^2 E_{\text{exc}}^2 + 2|C_{2m}| E_{\text{exc}} E_{\text{ref}} \cos(2m\Omega\tau + \theta_{2m}). \end{aligned} \quad (4)$$

The first and second terms in Eq. (4) correspond to the intensities of the ref-NIR pulse and the $2m^{\text{th}}$ sideband emission, respectively. The third term expresses the interference

1 between them. By changing the time delay τ , the interference term in Eq. (4) oscillates
 2 with a frequency of $2m\Omega$. This technique enables us to obtain the phase of the sideband
 3 emission θ_{2m} in addition to the amplitude $|C_{2m}|$. It is important that this heterodyne
 4 detection allows us to detect the sideband emission with higher sensitivity, which is
 5 explained in the following. Actually, from our measurement shown in Sec. II-B, the
 6 conversion efficiency of the exc-NIR intensity to the +2nd sideband emission intensity is
 7 estimated to be $|C_{+2}|^2 \approx 10^{-3}$ at a THz electric field strength of 10 kV/cm. On the other
 8 hand, the interference signal ratio $2|C_{+2}|$ is as high as 6×10^{-2} for $E_{\text{ref}} \approx E_{\text{exc}}$, which
 9 indicates a more than 10 times larger signal than that obtained with simply measuring
 10 the sideband emission intensity ($\sim 10^{-3}$).

11
 12 Figure 3(c) shows the spectra of the incident two-color NIR pulses with the excitation
 13 energy set to the 1s excitonic resonance ($\hbar\omega_{\text{exc}} = \varepsilon_{1s}$). For the heterodyne detection of
 14 the +2nd and +4th sideband emissions, we set the energy separation between the exc- and
 15 ref- NIR pulses to $2\hbar\Omega$ (orange solid line) and $4\hbar\Omega$ (blue dashed line), respectively. The
 16 corresponding transmitted NIR intensities under THz wave illumination ($E_{\text{THz}} = 7.7$
 17 kV/cm) show clear oscillations when scanning the delay time τ (Fig. 3(d)). The periods
 18 of the orange and blue oscillations are $2\pi/2\Omega$ and $2\pi/4\Omega$, respectively, in accordance
 19 with Eq. (4). The modulation strength of $\sim 6 \times 10^{-2}$ for the modulation frequency of
 20 2Ω (orange solid line) is also in good agreement with the estimation from Fig. 2(b).
 21 Hence, from the modulation depth ΔI_{2m} and the time lag of the signal peak $\Delta \tau_{2m}$
 22 depicted in Fig. 3(d), we can extract the amplitude $|C_{2m}|$ and the phase θ_{2m} of the $2m^{\text{th}}$
 23 sideband emission by using the relations $\Delta I_{2m} = 4|C_{2m}|(I_{\text{ref}}I_{\text{exc}})^{1/2}$ and $\Delta \tau_{2m} = \theta_{2m}/2m\Omega$.

24

25 **III. SIDEBAND EMISSION IN THE NONPERTURBATIVE** 26 **REGIME**

A. Excitation spectra of the +2nd sideband emission

In the following we discuss the +2nd sideband emission (C_{+2}), because this sideband can be clearly observed in both the perturbative and the nonperturbative regimes. To access the properties of the +2nd sideband emission, we performed the heterodyne detection for an energy separation of $2\hbar\Omega = 5$ meV between the exc- and ref-NIR pulses as shown in Fig. 4(a). We measured the amplitude spectra of the +2nd sideband emission ($|C_{+2}|$) at two different THz electric fields ($E_{\text{THz}} = 2.7$ kV/cm and 16 kV/cm) by scanning the exc- and ref-NIR photon energies ($\hbar\omega_{\text{exc}}, \hbar\omega_{\text{ref}} = \hbar\omega_{\text{exc}} - 5$ meV) around the 1s exciton resonance energy ε_{1s} . Experimentally obtained excitation spectra are shown in Fig. 4(b). The blue circles in Fig. 4(b) show that the amplitude spectrum has a sharp peak near ε_{1s} for a low THz field strength of $E_{\text{THz}} = 2.7$ kV/cm. At the higher field $E_{\text{THz}} = 16$ kV/cm, the spectral profile becomes broader and exhibits a redshift of around 2 meV as shown by orange squares in Fig. 4(b) [22], in contrast to what is expected in the perturbation theory, i.e., increase with E_{THz}^2 without spectral shape change. At 16 kV/cm, the Rabi energy ($\hbar\Omega_{\text{R}} = 7$ meV $\propto E_{\text{THz}}$) is comparable to the intra-excitonic transition energy $\varepsilon_{1s-2p} = 8$ meV, and these energies are much smaller than the ponderomotive energy ($U_{\text{p}} = 147$ meV $\propto E_{\text{THz}}^2$) [23]. Consequently, the interaction between the exciton and THz field causing the spectral shape change at 16 kV/cm (Fig. 4(b)) enters the nonperturbative regime where the RWA and perturbation theory are invalid.

Figure 4(c) plots the cycle-averaged absorption spectra obtained for different E_{THz} . Similar to the result observed for the sideband amplitude $|C_{+2}|$ (Fig. 4(b)), the 1s exciton absorption shows a significant spectral broadening at $E_{\text{THz}} = 16$ kV/cm, which can be explained by a reduction of the dephasing time of the THz-dressed 1s exciton. The

1 underlying physics of this nonperturbative behavior are discussed below. We found that
 2 the absorption spectrum starts to broaden at $E_{\text{THz}} = 4$ kV/cm, which is evidenced in Fig.
 3 4(d). Interestingly, the static field that is needed to ionize the 1s excitons is roughly
 4 estimated by $E_{\text{ion}} = \varepsilon_b/ea_B \sim \varepsilon_{1s-2p}/\hbar\Omega_R$, resulting in 4 kV/cm [24], which can be
 5 calculated when we use $\varepsilon_b \sim 8$ meV for the binding energy, and $a_B \sim 20$ nm for the Bohr
 6 radius of the 1s excitons (~ 20 nm), and the elementary charge e . This indicates that the
 7 spectral broadening observed in Fig. 4(b) originates from the distortion of the dressed 1s
 8 exciton due to the strong coupling with the continuum states (ionization).

9

10 On the other hand, the energy of the 1s excitonic resonance ε_{1s} shows only slight
 11 variations as shown in Fig. 4(d). We observed a redshift (< 0.3 meV) below 5 kV/cm
 12 which is due to the ac Stark effect, and a blueshift (< 0.6 meV) which is due to the
 13 dynamical Franz-Keldysh effect [25,26]. Since the redshift in absorption (< 0.3 meV) is
 14 much smaller than that observed for the $+2^{\text{nd}}$ sideband amplitude (Fig. 4(b); orange
 15 squares, ~ 2 meV), there is an additional effect on the $+2^{\text{nd}}$ sideband emission in the
 16 nonperturbative regime.

17

18 **B. Dressed excitons in the nonperturbative regime**

19 To understand the dressed exciton in the nonperturbative regime, we analyzed the
 20 data with the analytical expression for the $+2^{\text{nd}}$ sideband amplitude $|C_{+2}|$, which can be
 21 defined with [17,19,27]:

22

$$23 \quad C_{+2}(\omega_{\text{exc}}) \propto \chi_{+2}(\omega_{\text{exc}}) = \frac{|P_{CV}|^2}{\varepsilon_0 \hbar} \sum_{j,l} \frac{\phi_{j,l+2}^*(0) \phi_{j,l}(0)}{(\omega_{\text{exc}} - \varepsilon_j / \hbar - l\Omega) - i\Gamma_j}, \quad (5)$$

$$24 \quad \psi_j(\mathbf{r}, t) = \exp(-i\varepsilon_j t / \hbar) \sum_n \phi_{j,n}(\mathbf{r}) \exp(-in\Omega t), \quad (6)$$

25

1 where ϵ_0 and P_{CV} is the vacuum permittivity and interband dipole moment, χ_{+2} is the
 2 optical susceptibility of the +2nd sideband emission described with the dressed exciton
 3 ψ_j of state j (j being 1s, 2s, 2p, ...), $\phi_{j,n}$ is the n^{th} sideband state of ψ_j , r indicates the
 4 distance between the electron and hole, and ϵ_j and Γ_j are the quasi-energy and the
 5 dephasing rate of j -state exciton under THz wave illumination, respectively. The
 6 parameters of $\phi_{j,n}$, ϵ_j , and Γ_j in Eq. (5) depend on THz electric field, reflecting
 7 THz-exciton interactions such as ionization effect on dressed excitons.

8

9 Solid curves in Fig. 4(b) are the best fitted results of excitation spectra using Eq. (5)
 10 when we use $\phi_{j,l+2}^*(0)\phi_{j,l}(0)$ as fitting parameter. The fitting reproduces experimental
 11 results well in the energy region below the 1s excitonic resonance for both $E_{\text{THz}} = 2.7$
 12 kV/cm and 16 kV/cm. In the fitting calculation, we considered the dressed states of the
 13 1s and 2p exciton ($j = 1s$ and 2p) with n ranging from -2 to 2, corresponding to $(j,l) =$
 14 $(1s,0)$, $(1s,-2)$, and $(2p,-1)$ in Eq. (5), which are main contributions in the perturbative
 15 regime [17]. Also, ϵ_{1s} and Γ_{1s} are set to the values estimated by the fitting of the
 16 absorption spectra in Fig. 4(c), and assumed $\epsilon_{2p} = \epsilon_{1s} + 8$ meV and $\Gamma_{2p} = \Gamma_{1s}$. The fitting
 17 errors above $\epsilon_{1s} + 2\hbar\Omega$ can be attributed to the lack of contributions of higher-order
 18 excitonic and continuum state. The contributions of $(j,l) = (1s,-2)$ and $(1s,0)$ in Eq. (5)
 19 are respectively proportional to $\phi_{1s,0}^*(0)\phi_{1s,-2}(0)$ and $\phi_{1s,2}^*(0)\phi_{1s,0}(0)$, whose signs are
 20 opposite each other for the perturbation calculation result with $\hbar\Omega < \epsilon_{1s-2p}$ [17]. Thus,
 21 we can evaluate the ratio between $\phi_{1s,-2}(0)$ and $\phi_{1s,2}(0)$. At $E_{\text{THz}} = 2.7$ kV/cm, the value
 22 of $|\phi_{1s,-2}(0)|$ is much smaller than $|\phi_{1s,2}(0)|$ ($|\phi_{1s,-2}(0)/\phi_{1s,2}(0)| \sim 0.1$). But it becomes
 23 comparable to $|\phi_{1s,2}(0)|$ at $E_{\text{THz}} = 16$ kV/cm ($|\phi_{1s,-2}(0)/\phi_{1s,2}(0)| \sim 0.8$), meaning that the
 24 amplitude of the term which includes $\phi_{1s,-2}(0)$ in Eq. (5) (indicated by the yellow dashed
 25 line in Fig. 4(b)) becomes close to the term $\phi_{1s,2}(0)$ (the red dotted line in Fig. 4(b)) in
 26 the nonperturbative regime [7]. Since the peak energy of the term $\phi_{1s,-2}(0)$ is lower than

1 that of $\phi_{1s,2}(0)$ by $2\hbar\Omega = 5$ meV, the peak energy of the total sideband amplitude
 2 spectrum $|C_{+2}|$ becomes redshifted (the solid square and line in Fig. 4(b); ~ 2 meV) and
 3 larger than that seen in absorption (Figs. 4(c, d); < 0.3 meV).

4

5 THz-exciton interaction term $\hbar\Omega_R(t) = dE_{\text{THz}}(t) = dE_{\text{THz}}\cos(\Omega t)$ (instantaneous Rabi
 6 energy) can be split into two terms, which are respectively proportional to $\exp(-i\Omega t)$
 7 and $\exp(i\Omega t)$. These respectively correspond to co- and counter-rotating terms for 1s
 8 exciton. RWA is the approximation which neglects counter-rotating term, and is valid
 9 when THz excitation is resonant to the 1s-2p transition. Hence, $\phi_{1s,-2}(\mathbf{r})$, which is due to
 10 counter-rotating term, should be negligible compared with $\phi_{1s,2}(\mathbf{r})$, which is due to
 11 co-rotating term. Although our experimental condition is not resonant to 1s-2p transition
 12 ($\varepsilon_{1s-2p} = 8$ meV $> \hbar\Omega = 2.5$ meV), the perturbation calculation result for 2 level (1s and
 13 2p exciton) model shows that $|\phi_{1s,2}(0)|/|\phi_{1s,-2}(0)|$ is given by $(\varepsilon_{1s-2p} + \hbar\Omega)/(\varepsilon_{1s-2p} - \hbar\Omega) > 1$
 14 [17]. Our experimental results at 2.7 kV/cm in Fig. 4(b) shows $|\phi_{1s,-2}(0)| < |\phi_{1s,2}(0)|$. In
 15 contrast, $|\phi_{1s,-2}(0)|$ is almost the same as $|\phi_{1s,2}(0)|$ at 16 kV/cm, meaning that the RWA is
 16 invalid in the nonperturbative regime we studied.

17

18 Figure 4(e) shows the THz electric field dependences of the sideband amplitude $|C_{+2}|$
 19 at ε_{1s} and $\varepsilon_{1s-8\text{meV}}$ ($= \varepsilon_{1s} - 8.0$ meV). At ε_{1s} , where the contribution from $|\phi_{1s,2}(0)|$ is
 20 dominant, the amplitude starts to deviate from the power-law ($\propto E_{\text{THz}}^2$) for THz fields
 21 above $E_{\text{THz}} = 3$ kV/cm, which is almost the same field strength for ionization of the 1s
 22 exciton. On the other hand, at $\varepsilon_{1s-8\text{meV}}$, where the contribution of $|\phi_{1s,-2}(0)|$ is relatively
 23 strong, the amplitude obeys the power-law up to 10 kV/cm. Since the energy of $\phi_{1s,2}(\mathbf{r})$
 24 (*i.e.*, $\varepsilon_{1s} + 2\hbar\Omega$) is closer to the continuum than that of $\phi_{1s,-2}(\mathbf{r})$ ($\varepsilon_{1s} - 2\hbar\Omega$), the field
 25 ionization effect is more pronounced for $\phi_{1s,2}(\mathbf{r})$, and this causes the saturation of
 26 $|\phi_{1s,2}(0)|$ at high THz fields ($|\phi_{1s,2}(0)| \sim |\phi_{1s,-2}(0)|$). Figure 4(f) plots the phase shift $\Delta\theta_{+2}$

1 of the +2nd sideband emission at ϵ_{1s} and $\epsilon_{1s-8meV}$ as a function of E_{THz} . Here, the phase
 2 shift is defined with $\Delta\theta_{+2}(E_{THz}) = \theta_{+2}(E_{THz}) - \theta_{+2}(E_{THz} = 16 \text{ kV/cm})$. Below 5 kV/cm,
 3 the phase of the sideband signal at $\epsilon_{1s-8meV}$ exhibited a shift close to π , *i.e.*, sign
 4 inversion of the sideband emission. On the other hand, the phase for the signal at ϵ_{1s} is
 5 less sensitive to the THz electric field. The phase shifts evaluated from the fitting with
 6 Eq. (5) (Fig. 4(f); open circles and open squares correspond to ϵ_{1s} and $\epsilon_{1s-8meV}$,
 7 respectively) reproduce the direct experimental results and confirm the validity of our
 8 model, *i.e.*, the relative increase of the amplitude of $\phi_{1s,-2}(0)$, whose sign is opposite to
 9 that of $\phi_{1s,-2}(0)$, is responsible for the observed sideband emission properties in the
 10 nonperturbative regime [28].

11

12

IV. SUMMARY

13

14

15

16

17

18

19

20

21

22

23

In summary, we investigated the sideband emissions in the nonperturbative regime. We demonstrated that the heterodyne detection of the sideband emission is a powerful tool to access the optical susceptibility of the THz dressed exciton. The dependences of the +2nd sideband emission on the THz electric field strength revealed that the field ionization of the 1s excitons causes a change in the energy spectrum of the THz-dressed exciton, which is related to reduction of the dephasing time and breakdown of RWA in the nonperturbative regime. The further understanding of the nonperturbative nonlinear optical processes including phase information paves the way for sub-cycle control and synthesis of optical pulses.

1 **ACKNOWLEDGEMENTS**

2 This study was supported by PRESTO Grant JPMJPR1427 from JST, Grant-in-Aid for
3 JSPS fellows (17J09419), and KAKENHI (26286061, 17H06228, 26247052,
4 17H06124) from JSPS. The work at Princeton University was also funded by the
5 Gordon and Betty Moore Foundation through the EPiQS initiative Grant GBMF4420,
6 and by the National Science Foundation MRSEC Grant DMR-1420541.

7

1 **REFERENCES**

- 2 [1] F. Krausz, M. I. Stockman, *Nature Photon.* **8**, 205 (2014).
- 3 [2] W. Kuehn, P. Gaal, K. Reimann, M. Woerner, T. Elsaesser, and R. Hey, *Phys. Rev.*
4 *Lett.* **104** 161201(2010).
- 5 [3] S. Ghimire, A. D. DiChiara, E. Sistrunk, P. Agostini, L. F. DiMauro, and D. A. Reis,
6 *Nat. Phys.* **7**, 138 (2011).
- 7 [4] A. Schiffrin, T. Paasch-Colberg, N. Karpowicz, V. Apalkov, D. Gerster, S.
8 Mühlbrandt, M. Korbman, J. Reichert, M. Schultze, S. Holzner, J. V. Barth, R.
9 Kienberger, R. Ernstorfer, V. S. Yakovlev, M. I. Stockman, and F. Krausz, *Nature*
10 **493**, 70 (2013).
- 11 [5] M. Wegener, *Extreme Nonlinear Optics* (Springer-Verlag, Berlin/Heidelberg, 2005).
- 12 [6] H. Haug, and S. W. Koch, *Quantum Theory of the Optical and Electronic Properties*
13 *of Semiconductors* (World Scientific, Singapore, 2009).
- 14 [7] R. A. Kaindl, M. A. Carnahan, D. Hägele, R. Lövenich, and D. S. Chelma, *Nature*
15 **423**, 734 (2003).
- 16
- 17 [8] S. G. Carter, V. Birkedal, C. S. Wang, L. A. Coldren, A. V. Maslov, D. S. Citrin,
18 and M. S. Sherwin, *Science* **310**, 651 (2005).
- 19 [9] M. Wagner, H. Schneider, D. Stehr, S. Winnerl, A. M. Andrews, S. Schartner, G.
20 Strasser, and M. Helm, *Phys. Rev. Lett.* **105**, 167401 (2010).
- 21 [10] K. Uchida, H. Hirori, T. Aoki, C. Wolpert, T. Tamaya, K. Tanaka, T. Mochizuki, C.
22 Kim, M. Yoshita, H. Akiyama, L. N. Pfeiffer, K. W. West, *Apply. Phys. Lett.* **107**,
23 221106 (2015).
- 24 [11] H. Hirori, M. Nagai, and K. Tanaka, *Phys. Rev. B* **81**, 081305(R) (2010).
- 25 [12] B. Ewers, N. S. Köster, R. Woscholski, M. Koch, S. Chatterjee, G. Khitrova, H. M.
26 Gibbs, A. C. Klettke, M. Kira, and S. W. Koch, *Phys. Rev. B* **85**, 75307 (2012).
- 27 [13] J. Kono, M. Y. Su, T. Inoshita, T. Noda, M. S. Sherwin, S. J. Allen, and Jr., H.
28 Sakaki, *Phys. Rev. Lett.* **79**, 1758 (1997).
- 29 [14] M. Wagner, H. Schneider, S. Winnerl, M. Helm, T. Roch, A. M. Andrews, S.
30 Schartner, and G. Strasser, *Apply. Phys. Lett.* **94**, 241105 (2009).
- 31 [15] B. Zaks, R. B. Liu, and M. S. Sherwin, *Nature* **483**, 580 (2012).

- 1 [16] F. Langer, M. Hohenleutner, C. P. Schmid, C. Poellmann, P. Nagler, T. Korn, C.
2 Schüller, M. S. Sherwin, U. Huttner, J. T. Steiner, S. W. Koch, M. Kira, and R.
3 Huber, *Nature* **533**, 225 (2016).
- 4 [17] K. Uchida, T. Otobe, T. Mochizuki, C. Kim, M. Yoshita, H. Akiyama, L. N. Pfeiffer,
5 K. W. West, K. Tanaka, and H. Hirori, *Phys. Rev. Lett.* **117**, 277402 (2016).
- 6 [18] T. Otobe, Y. Shinohara, S. A. Sato, and K. Yabana, *Phys. Rev. B* **93**, 045124
7 (2016).
- 8 [19] K. Johnsen and A. P. Jauho, *Phys. Rev. Lett.* **83**, 1207 (1999).
- 9 [20] K. -L. Yeh, M. C. Hoffmann, J. Hebling, and K. A. Nelson, *Appl. Phys. Lett.* **90**,
10 171121 (2007).
- 11 [21] H. Hirori, A. Doi, F. Blanchard, and K. Tanaka, *Appl. Phys. Lett.* **98**, 091106
12 (2011).
- 13 [22] B. Zaks, H. Banks, and M. S. Sherwin, *Appl. Phys. Lett.* **102**, 012104 (2013).
- 14 [23] We use envelope Rabi energy $\hbar\Omega_R = dE_{\text{THz}}$, which characterizes response of
15 dressed exciton within RWA. Here, d is the transition dipole moment of the 1s-2p
16 transition, and we used $d = 43 e\text{\AA}$, which has been theoretically estimated from the
17 two-dimensional exciton model (see. Ref. 6 and M. Shinada and S. Sugano, *J. Phys.*
18 *Soc. Jpn.* **21**, 1936 (1966)). The ponderomotive energy U_p is defined as $U_p =$
19 $= e^2 E_{\text{THz}}^2 / 4m^* \Omega^2$, where e is the elementary charge, m^* ($=0.054m_0$) is the reduced
20 mass of the exciton, and m_0 is the free electron mass. The ratio between U_p and
21 binding energy of a bounded state ϵ_B given by $\text{KP} = \sqrt{\epsilon_B / 2U_p}$ is called Keldysh
22 parameter (see Ref. 5). When KP becomes smaller than one, ionization is described
23 as tunneling process instead of multi-photon process.
- 24 [24] D. A. B. Miller, D. S. Chemla, T. C. Damen, A. C. Gossard, W. Wiegmann, T. H.
25 Wood, and C. A. Burrus, *Phys. Rev. B* **32**, 1043 (1985).
- 26 [25] K. B. Nordstrom, K. Johnsen, S. J. Allen, A. P. Jauho, B. Birnir, J. Kono, T. Noda,
27 H. Akiyama, and H. Sakaki, *Phys. Rev. Lett.* **81**, 457 (1998).
- 28 [26] M. Teich, M. Wagner, D. Stehr, H. Schneider, M. Helm, C. N. Böttge, A. C.
29 Klettke, S. Chatterjee, M. Kira, S. W. Koch, G. Khitrova, and H. M. Gibbs, *Phys.*
30 *Rev. B* **89**, 115311 (2014).
- 31 [27] J. H. Shirley, *Phys. Rev.* **138**, B979 (1965).

1 [28] By using $\phi_{j,l+2}^*(0)\phi_{j,l}(0)$, ϵ_j , and Γ_j deduced from the experimental results (Fig.
2 4(d)), we calculated phase of 2nd sideband emission $\theta_{+2} = \arg(C_{+2})$. Here, in order to
3 interpolate THz electric field dependence of $\phi_{i,l+2}^*(0)\phi_{i,l}(0)$, we assumed
4 $\phi_{1s,2}^*(0)\phi_{1s,0}(0) = AC_{+2}(\epsilon_{1s})/\Gamma_{1s}$ and $\phi_{1s,0}^*(0)\phi_{1s,-2}(0) = BC_{+2}(\epsilon_{1s-8\text{meV}})/\Gamma_{1s}$ according to Eq.
5 (5). By using experimentally obtained Γ_{1s} , $|C_{+2}(\epsilon_{1s})|$, $|C_{+2}(\epsilon_{1s+8\text{meV}})|$, and adjusting
6 scales A and B , we obtained THz electric field dependence of $\phi_{i,l+2}^*(0)\phi_{i,l}(0)$ for the
7 whole range which is good agreement with that extracted from the fitting in Fig.
8 4(b) (THz electric field dependence of $\phi_{2p,1}^*(0)\phi_{2p,-1}(0)$ is deduced from the linear
9 interpolation).

10

1 **Figure captions**

2 FIG. 1. (a) Experimental setup for coherent detection of THz-induced sideband
3 emissions from a GaAs/AlGaAs MQW. The NIR pulse passed through a small hole in
4 the parabolic mirror used to focus the THz waves. Both polarizations of the THz and
5 NIR waves were linear and parallel. BS: non-polarized beam splitter, OC: optical
6 chopper, HWP: half wave plate, BPF: bandpass filter (0.6 THz), and WGPs: wire-grid
7 polarizers. (b) Temporal profile of the THz electric field measured by EO sampling with
8 a 400- μm -thick GaP crystal. (c) Fourier amplitude spectrum of the THz wave. (d)
9 Absorption spectrum of the GaAs/AlGaAs MQW at 10 K defined as $-\log(I_{\text{sam}}/I_{\text{ref}})$,
10 where I_{sam} and I_{ref} are transmitted intensities with and without sample. The background
11 term due to the multiple reflections within the sample is excluded. HH indicates a
12 heavy-hole exciton.

13

14 FIG. 2. (a) Schematics of the excitonic energy states (left) and the sideband emissions
15 from the THz dressed exciton (right). The 1s and 2s exciton states lie below the higher
16 excitonic and continuum states (grey shaded area). (b) Sideband spectrum under THz
17 wave illumination with $E_{\text{THz}} = 10$ kV/cm. The red dashed line is the incident NIR
18 spectrum that was narrowed by the pulse shaper with a single slit. The orange and
19 brown solid lines indicate the spectra of three sideband emissions ($\pm 2^{\text{nd}}$ and $+4^{\text{th}}$ order,
20 respectively). The vertical scales are respectively multiplied by 200 and 2000. The gray
21 shaded area shows absorption spectrum.

22

23 FIG. 3. (a) Schematic diagram of coherent sideband detection in the frequency domain.
24 exc- and ref- indicate the NIR waves that were used for the excitation of the system and
25 the reference for the heterodyne detection, respectively. (b) Schematic diagram of
26 coherent sideband detection in the time domain. The beating frequency of the NIR pulse

1 corresponds to the energy separation between the exc- and ref-NIR wave in (a). The
2 time delay τ between the THz and NIR pulses is defined as the difference between the
3 peak positions of the THz electric field and the NIR pulse in the time domain. (c) NIR
4 transmission spectra obtained for energy separations set to $2\hbar\Omega$ (orange solid line) and
5 $4\hbar\Omega$ (blue dashed line). The gray area shows the absorption spectrum. (d) Transmitted
6 NIR intensities as a function of delay time τ at $E_{\text{THz}} = 7.7$ kV/cm. The orange solid and
7 blue dashed lines correspond to the NIR signal intensities shown in (c). ΔI_{2m} and $\Delta\tau_{2m}$
8 ($2m = +2$ and $+4$) are modulation depth and time lag of the signal peak of the $2m^{\text{th}}$
9 sideband emission, respectively. Intensities are normalized by the respective
10 time-averaged intensities over the cycle of THz wave $2\pi/\Omega$.

11

12 FIG. 4. (a) Schematic diagram of the heterodyne scanning procedure. (b) $+2^{\text{nd}}$ -order
13 sideband amplitude spectra $|C_{+2}(\omega_{\text{exc}})|$. $\varepsilon_{1s+2\hbar\Omega}$ and $\varepsilon_{1s-2\hbar\Omega}$ indicate the energy of $\varepsilon_{1s} +$
14 $2\hbar\Omega$ and $\varepsilon_{1s} - 2\hbar\Omega$, respectively. The light-blue circles and orange squares are the
15 measurement results obtained for $E_{\text{THz}} = 2.7$ kV/cm and 16 kV/cm, respectively. The
16 blue and brown solid lines are the fitting results for $|C_{+2}|$ using Eq. (5). The dotted and
17 dashed lines correspond to $|C_{+2}|$ for $(j,l) = (1s,0)$ and $(1s,-2)$. The data of $|C_{+2}|$ for $(j,l) =$
18 $(2p,-1)$, which has a peak around $\varepsilon_{1s+2\hbar\Omega}$, is not shown in the graph. (c) Absorption
19 spectra without THz illumination (black solid line), and for THz electric field strengths
20 of $E_{\text{THz}} = 2.7$ kV/cm (light blue solid line), and $= 16$ kV/cm (orange solid line). (d) THz
21 field dependence of the peak energy shift (black squares) and spectral width (red
22 circles) of the 1s exciton absorption evaluated by Lorentzian fitting. The dashed line is
23 the calculation result of the cycle-averaged field ionization rate from Ref. [24]. (e) $+2^{\text{nd}}$
24 sideband amplitude $|C_{+2}|$ as a function of E_{THz} . The green circles and blue squares
25 respectively indicate measurement results for $\hbar\omega_{\text{exc}} = \varepsilon_{1s}$ and $\varepsilon_{1s-8\text{meV}}$. The black dashed
26 lines are proportional to E_{THz}^2 . (f) Phase shift of the $+2^{\text{nd}}$ -order sideband emission at $\hbar\omega_{\text{exc}}$

1 = ε_{1s} and $\varepsilon_{1s-8meV}$ (green solid circles and blue solid squares, respectively). Green open
2 circles and blue open squares indicate the phase shift deduced from the fitting results in
3 (b) by using Eq. (5).

4

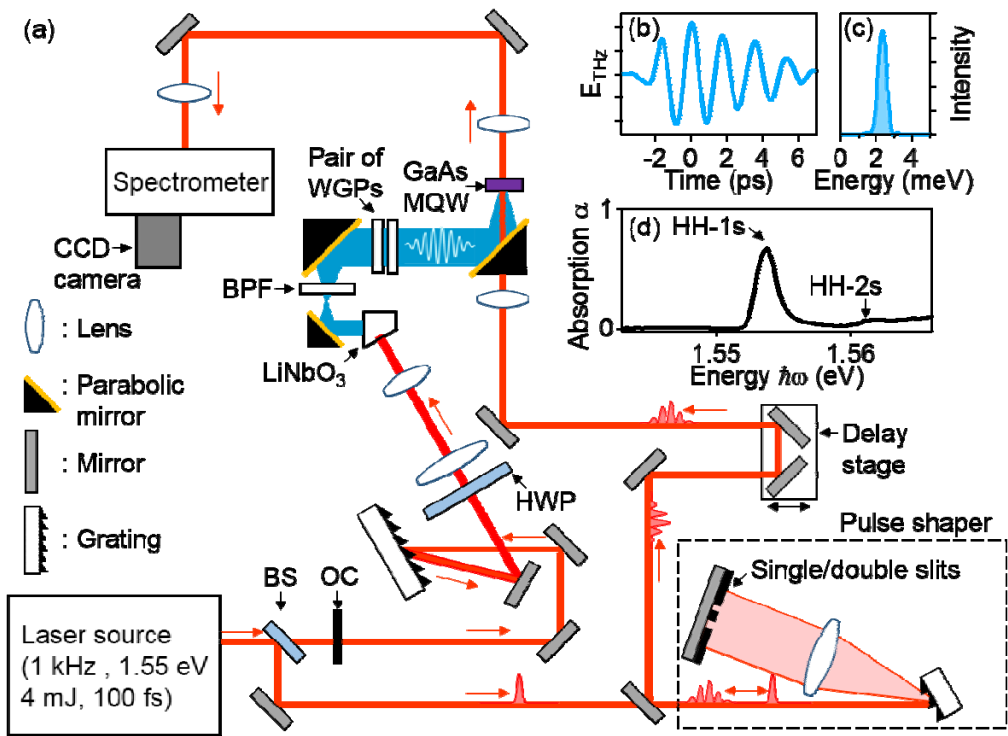
5

6

7

1 **FIG. 1**

2
3
4
5
6
7
8
9
10
11
12
13
14
15
16
17
18
19
20
21
22
23
24
25
26



K. Uchida

1

2 **FIG. 2**

3

4

5

6

7

8

9

10

11

12

13

14

15

16

17

18

19

20

21

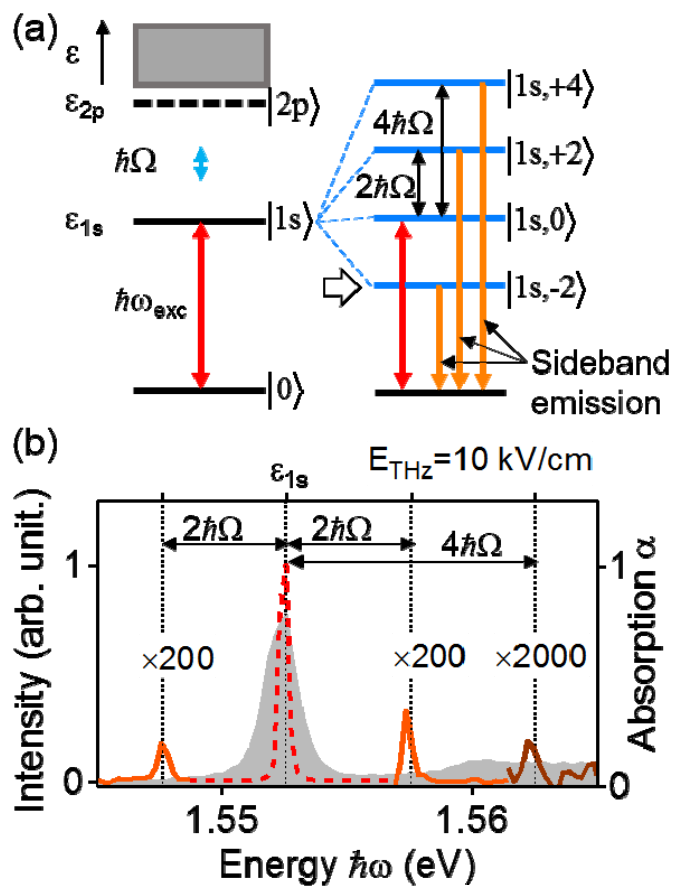
22

23

24

25

26



1

2

3 **FIG. 3**

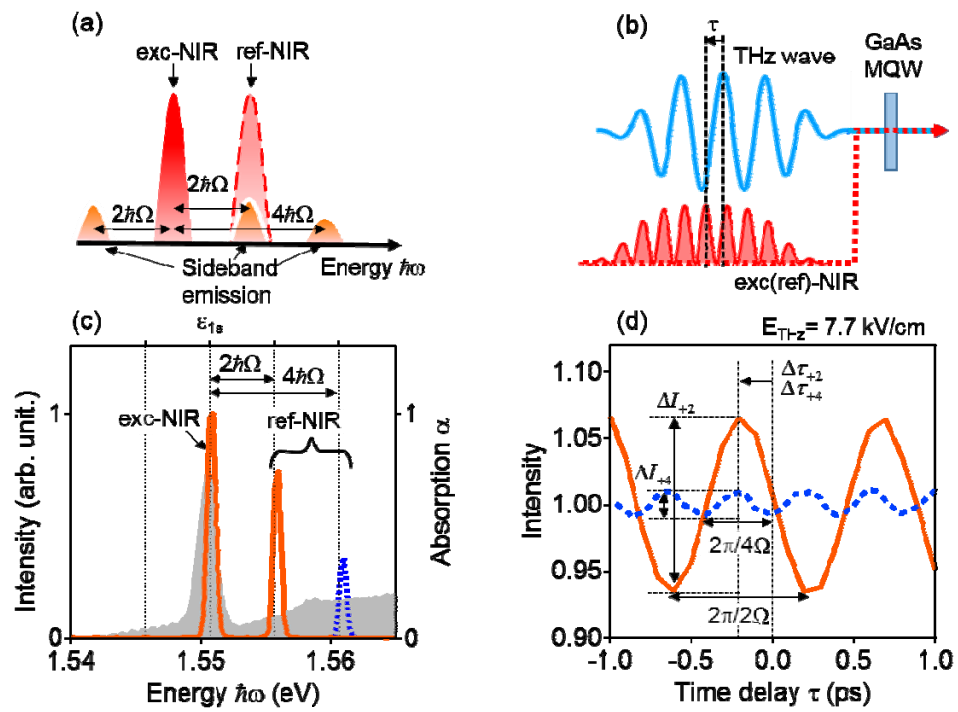
4

5

6

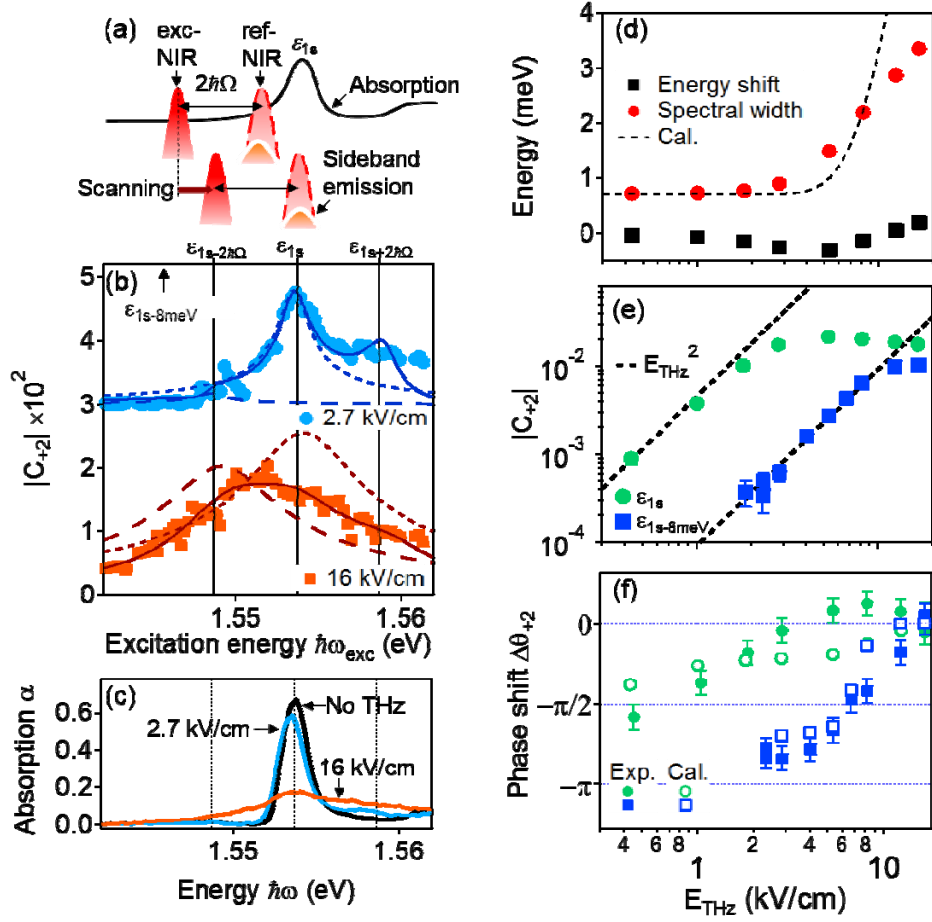
7

K. Uchida



1 **FIG. 4**

2
3
4
5
6
7
8
9
10
11
12
13
14
15
16
17
18
19
20
21
22
23



K. Uchida